A case study of wind farm effects using two wake parameterizations in WRF (V3.7) in the presence of low level jets

Xiaoli G. Larsén[1] and Jana Fischereit[1]

[1]Wind Energy Department, Technical University of Denmark, Frederiksborgvej 399, Building 125, 4000 Roskilde, Denmark
Correspondence: Xiaoli G. Larsén (xgal@dtu.dk)

Abstract. While the wind farm parameterization by Fitch et al. (2012) in Weather Research and Forecasting (WRF) model has been used and evaluated frequently, the Explicit Wake Parameterization (EWP) by Volker et al. (2015) is less well explored. The openly available high frequency flight measurements from Bärfuss et al. (2019) provide an opportunity to directly compare the simulation results from the EWP and Fitch scheme with in situ measurements. In doing so, this study aims to compliment
5 the recent study by Siedersleben et al. (2020) by (1) comparing the EWP and Fitch schemes in terms of turbulent kinetic energy (TKE) and velocity deficit, together with FINO 1 measurements and Synthetic Aperture Radar (SAR) data and (2) exploring the interactions of the wind farm with Low Level Jets.

   Both the Fitch and the EWP schemes can capture the mean wind field in the presence of the wind farm consistently and well. However, their skill is limited in capturing the flow acceleration along the farm edge. TKE in the EWP scheme is significantly
10 underestimated, suggesting that an explicit turbine-induced TKE source should be included in addition to the implicit source from shear. The position of the LLJ nose and the shear beneath the jet nose are modified by the presence of wind farms.

1   Introduction

Offshore wind energy has been developing fast in recent years. Consequently, wind farms are growing bigger and bigger in
15 both capacity and spatial sizes. For instance in the North Sea, a farm can extend over tens of kilometers, sometimes forms clusters with neighbouring farms, resulting in a cluster size of several thousands of km^2, e.g. the Hornsea area (7240 km^2); see www.4coffshore.com for an overview of wind farms. Wind turbines and farms extract momentum from the atmospheric flow and interact with it, causing reduction in wind speed and increase in turbulence in the wake regions. To assess such impact over areas with sizes of modern farm-clusters, mesoscale modeling has shown to be a useful tool in including synoptical and
20 mesoscale wind variability. Several mesoscale models have been used to study the wind farm effects, and the Weather Research and Forecasting (WRF) model (Skamarock et al., 2007) is the most-used mesoscale model, according to a recent review by Fischereit et al. (2020). In connection with the use of WRF, the wind farm parameterization (WFP) scheme, called the Fitch scheme here (Fitch et al., 2012) and the explicit wake parameterization (Volker et al., 2015), called the EWP scheme here, are

the two most commonly applied explicit wind farm parameterizations. Most publications used the Fitch scheme (Fischereit

25   et al., 2020).

The Fitch scheme has long been implemented in WRF, which makes it convenient for users, regarding further development, investigation, application and validation. The EWP scheme, on the other hand, is not included in the official WRF repository and it has not been explored and validated as frequently. Studies comparing the two schemes on the calculation of the turbulent kinetic energy (TKE) are thus limited. Volker et al. (2015); Volker et al., Catton (2020), Pryor et al. (2020) and Shepherd et al.

30   (2020) are the few, with the first two addressing offshore wind farms, and the last two onshore wind farms. These studies consistently show that the Fitch scheme provides wind-farm-induced TKE significantly larger than the EWP scheme does. The two schemes differ with respect to their treatment of turbine-induced forces in the momentum equation as well as to their treatment of wind farms as a source of TKE. In the Fitch scheme, the turbine-induced force is represented by a local thrust force (as a function of the thrust coefficient) acting on the turbine-swept area. In the EWP scheme, a grid cell averaged drag force

35   is applied that accounts for a sub-grid scale vertical wake expansion based on the concept from Tennekes and Lumley (1972). With respect to TKE, in the Fitch scheme wind turbines are treated as an explicit source of TKE. By neglecting mechanical losses, turbine-induced TKE is a function of the difference between the power and the thrust coefficients. While in the EWP scheme, no explicit source term is considered and the turbine-induced TKE arises solely the shear production in the wind farm wake.

40   TKE describes the fluctuation of kinetic energy and it is related to the turbulence, which is a key wind-energy application parameter. The modelling of wind-farm-induced TKE from the Fitch scheme has been previously evaluated in a number of case studies with measurements from profiling lidars (Lee and Lundquist, 2017a, b). With considerable uncertainties embedded with the lidar technique, Lee et al. showed that TKE from the Fitch scheme can capture the general pattern from the measurements. Siedersleben et al. (2020) (hereinafter S2020) used in situ high-frequency airborne measurements to evaluate TKE from the

45   Fitch scheme in WRF for three case studies. They found that the Fitch scheme overestimates the TKE on the upwind side of the wind farm and underestimates it on the downwind side. They also noted that capturing the background meteorology is crucial to evaluate the performance of the scheme, which they managed only within their case study II.

During the case study II of S2020, there were Low Level Jets over the area. Wagner et al. (2019) showed that LLJs are a common phenomenon in this area: by analysing of one-and-an-half year of campaign measurements using lidar and a passive

50   microwave radiometer over the Southern North Sea they found that LLJs occurred on about 65% of the days during the campaign. Flow from the southwest (such as case II) is one of the favourable conditions in forming LLJs in this area. Wagner et al.'s data show that LLJs in association with flow from the south and the southwest typically have the jet nose (wind speed maximum) height from 200 m to 300 m. This is expected to have non-negligible impact on the turbine performance, which is related to not only the increased wind resource, but also to the unusual vertical distribution of wind shear, with enhanced shear

55   beneath the jet nose and negative shear above it. Thus, turbulence will also be affected, causing considerable uncertainties in the estimation of relevant key parameters, such as load. It has not yet been documented in the literature how the structure of LLJ is affected by the presence of large wind farms. There also lack published studies showing how the wind farm wakes are affected by the presence of LLJs.

This study takes advantage of the open source flight data from Bundesnetzagentur (2019) and Bärfuss et al. (2019a), and

60 follows up on the recently publication by S2020. The purpose is thus two folds: (1) S2020 pointed out: "For comparison, it would be interesting to simulate case study II with the wind farm parameterization of Volker et al. (2015)". With the availability of the high frequency velocity measurements, this study contributes to this knowledge gap through revisiting the case study II in S2020 and comparing the EWP and the Fitch schemes in the WRF modeling. This study will thus also be the first to use measurements to verify the calculations of TKE using the EWP scheme. (2) Studying "case study II" from 14 Oct 2017 in

65 S2020 to examine the the wind characteristics under the impact of both wind farm wakes and LLJs.

The methods used here are introduced in the next section, including the measurements and the WRF model setup. The results will be presented in Sect. 3, followed by discussions in Sect. 4 and conclusions in Sect. 5 .

2 Method

The case study from 14 Oct 2017 will be modeled here using WRF applying both the EWP and Fitch scheme; details of the

70 model setup are given in Sect. 2.2. The model output will be analyzed together with various measurements in line with S2020. These measurements are introduced in Sect. 2.1. In this study, time in both the measurements and the modeled data is presented in UTC.

2.1 Measurements

Case study II from S2020 took place on 14 Oct 2017. Along with warm air advection from land to sea, LLJs formed. Wind

75 farm wakes were generated, which is obvious from the Synthetic Aperture Radar (SAR) data as the streaks of reduced wind speed, as shown in their Fig. 4a, which is re-produced here in Fig. 1.

Three types of measurements are used here to study this event. The first is the open access measurements published in Bärfuss et al. (2019a), Lampert et al. and Platis et al. (2018), and analyzed in S2020. The measurements are briefly introduced here and their details can be found in these publications. The flight track on the 14 Oct 2017 is re-produced here as Fig. 2.

80 The transect-flight over the wind farm is indicated in cyan and labelled by "a". The colored blocks labeled with digits 1 to 6 indicate profiling flights along the track. The start and end time of each profiling flight are provided in Table 1.

The flight data include: (1) Vertical profiles of a number of variables, including temperature T (K), pressure P (hpa), and the along-wind, cross-wind and vertical-wind components, u, v and w, respectively, from these profiling flights from the surface to about 600 m. Following S2020, we calculated the potential temperature θ from temperature T and pressure P using

85 $\theta = T \cdot (P_0/P)^{0.2859}$, where $P_0 = 1000$ hPa. These profile data provide background information, and are not affected by wind farm wakes (see Fig. 2 for their position relative to the farms during the flight period). We call these data "profile-flight"; (2) Horizontal flight data for u, v and w, among other variables, above the wind farm at 250 m; these data are affected by the wind farms. We call these data "transect-flight".

We downloaded the flight data from Bärfuss et al. (2019a). The flight measurements are sampled at a frequency of 100 Hz,

90 corresponding to a horizontal resolution of 0.66 m (Platis et al., 2018). The flights over Godewind 1 were conducted at an

elevation of 250 m, slightly above the rotor top (187 m, with hub height 110 m and diameter 154 m, see also Table 2). For the analyses of the vertical profile, we averaged the profile-flight data over a vertical interval of 10 m. For the transect-flight data, TKE is calculated following $TKE = 0.5 \cdot (\sigma_u^2 + \sigma_v^2 + \sigma_w^2)$, where σ_u, σ_v and σ_w are standard deviation of the three wind components. The calculation is done over windows of both 2 km and 1.5 km. The choice of the window length is made

95 following the argument in Platis et al. (2018) for the turbulence length scales, where they used 1.5 km. Given the background wind speed approximately 10 - 15 ms^{-1}, the time scales over both 2 km and 1.5 km are on the order of a couple of minutes, which is a reasonable integral time scale. Our analyses was made using both scales, but are presented only for 2 km, in order to match the spatial horizontal resolution of the WRF model; details are given in Sect. 3.

Wind farms included in the WRF modeling are shown in a larger map in Fig. 3a, and the details of these farms are provided

100 in Table 2. Figure 3b is a close-up of Fig. 3a, with the two closest consecutive rows of WRF model grids shown over the Godewind 1 farm (in black and red), covering the flight track-a (in cyan). An additional row of the WRF grid points (in blue) is chosen east of the farm in the wake affected area. These three rows are denoted as transect-black, transect-red and transect-blue according to the colors in our analysis. They will be used for analyzing the transect distribution of wind speed and TKE.

The second measurement type is from the FINO 1 mast. In Fig. 3b, the location of the FINO 1 mast is marked with $F1$. Note

105 that with wind direction from about 240°, FINO 1 is in the wake of the upstream wind farm Borkum Riffgrund. The 10-min values of wind speed from 30 m to 100 m, and wind direction from 30 m to 90 m on 14 Oct are used.

The third measurement type is the SAR data. The wind farm wakes can be seen as reduced wind speed in Fig. 1a, where the wind field was retrieved from ENVISAT SAR at 17:17 UTC on 14 Oct 2017. The retrieval uses the empirical relationship between the 10-m wind speed and the radar backscatter that depends on the local wind-generated wind waves (Valenzuela,

110 1978; Hersbach et al., 2007). The spatial resolution of the SAR data shown in Fig. 1a is about 500 m. Fig. 1a is made from more than one SAR scenes; even though the farm wake pattern is continuous across scenes, there seems to be an artificial change in wind speed east of about 6.5°E, which was also present in S2020. Due to these uncertainties, the SAR data will only be analyzed qualitatively.

2.2 Modeling

115 LLJs over the Southern North Sea are mostly associated with relatively warm continental air advected over cooler sea surface, where a stable internal boundary layer develops, causing quasi-frictional decoupling and an acceleration of air mass. The phenomena are rather common in coastal regions and they have been studied in a long list of literature, e.g. Smedman et al. (1993, 1995); Wagner et al. (2019); Kalverla et al. (2019). It is challenging to accurately simulate LLJs using WRF, where important elements include model domain configuration, initialization and boundary forcing data, horizontal and vertical spatial

120 resolutions, PBL schemes etc. (Nunalee and Basu, 2014; Wagner et al., 2019; Kalverla et al., 2019; Siedersleben et al., 2020; Tay et al., 2020). Different studies have suggested different best candidate elements for setting up WRF in order to capture the LLJ characteristics. Our choices of these key elements are in agreement with the general recommendation in literature. This includes (1) horizontal spatial resolution of 2 km in the innermost model domain; (2) a large number of vertical model levels, here 80 with 21 in the lowest 200 m; (3) initial and boundary forcing using ERA 5 data; (4) MYNN PBL scheme, which was

125 shown to outperform the others in Tay et al. (2020), while in Nunalee and Basu (2014), MYNN performed fine but the best candidate was QNSE. Since the Fitch scheme can only be used in connection with MYNN to calculate TKE developments, this scheme was used.

We use WRF version 3.7 to simulate this case. The model contains three nested domains (Fig. 4) and the spatial resolutions are 18, 6 and 2 km for domain I, II and III, respectively. Following the suggestion by S2020 and in agreement with other

130 sensitivity studies (Tomaszewski and Lundquist, 2020; Lee and Lundquist, 2017a), we use 80 vertical layers with 21 layers below 200 m with a thickness of about 10 m. We use MYNN2.5 Planetary Boundary Layer (PBL) scheme Nakanishi and Niino (2009), Thompson microphysics scheme Thompson et al. (2004), RRTMG long wave and short wave radiation physics schemes Iacono et al. (2008). The Kain-Fritsch cumulus scheme (Kain and Fritsch, 1993) is used for domain I but it is deactivated for domain II and III. The Corine land use data from 2017 are used. ERA-5 data on pressure levels are used as the initial and

135 boundary forcing for WRF. In addition, the OSTIA SST data, which is produced daily at a resolution of $(1/20)°$, approximately 5 km (Stark et al., 2007) was used.

The WRF simulation starts at 6:00 on 14 Oct 2017 and runs to the end of day. The simulation captures the development of LLJs and it is sufficiently long to be compared to the available measurements. The simulation has been run in three modes, one with the Fitch scheme, one with the EWP scheme and one without wind farms (NWF). The outputs are 10-min instanta-

140 neous values from each time step, including the longitudinal wind component U, the meridional wind component V, potential temperature θ and QKE, from which we further calculated the wind speed, the wind direction and TKE ($0.5 \cdot QKE$). In connection with the Fitch scheme for the wind-farm-induced TKE, there are two options: one with the advection of it turned off and one with it turned on. For most studies in the literature, including S2020, the advection of the wind-farm-induced TKE has been set to be off, due to a bug in WRF that would give unrealistic values, as reported in Archer et al. (2020). Archer et al.

145 (2020) fixed this bug and experimented with a coefficient C_{TKE}, the wind-farm-induced TKE factor, in connection with the advection scheme. The factor C_{TKE} is used to adjust the magnitude of TKE as described in the Fitch scheme and it is recommended to be less than 1 to respond to their Large Eddy Simulation experiments. In this study, when using the Fitch scheme, the default uses farm-induced TKE-advection off, with $C_{TKE} = 1$, which is the same as in S2020. Further experiments using this TKE-advection on with $C_{TKE} = 0.25$ and 1 are briefly compared to the default and measurements (see Section 4). Since

150 EWP does not have a similar term in the TKE-equation that is a function of turbines, this issue is absent.

The development of LLJs is sensitive to the domain configuration. In our experiments, LLJs failed to develop when the southern land area was too small, likely caused by an unsuccessful development of the stable internal boundary layer associated with warm air advection. This problem is solved by increasing the land area in the southern part.

The turbine information includes location, hub height, rotor diameter, power coefficient and thrust coefficient. In our sim-

155 ulation, the locations of the turbines from the wind farms shown in Fig. 3 are obtained from three different sources: (1) Bundesnetzagentur (2019) for most German wind farms (2) Energistyrelsen (2020) for Danish wind farms and (3) for other wind farms not included in these two data sets turbine locations have been derived from SAR images in (Langor, 2019) and manually corrected to fit the wind farm shapes from emodnet (Emodnet, 2020). For the simulations in this study only wind farms built before 2018 are included in accordance with the simulated date (Table 2). In S2020, three types of turbine are used,

160 with Siemens SWT 6.0-154 for Godewind 1 and 2, Siemens SWT 3.6-120 for Meerwind Süd Ost and Senvion 6.2 for OWP Nordsee Ost (see Table 3 in S2020). They used the thrust and power coefficients of Siemens SWT 3.6-120 onshore for all turbines implemented in the simulation. In our study, we used the turbine type for each wind farm from sources above (Table 2). Power and thrust curves for each turbine have been taken from Langor (2019) or from WAsP (http://www.wasp.dk/). We used an initial length scale of 1.6 for the EWP scheme related to the subgrid scale vertical wake expansion.

3   Results and Analysis

3.1   Low Level Jets

With warmer air moving from the land over the sea in the direction of about 240°, a stable boundary layer (SBL) developed over the sea, as can be seen from the profile-flight data, shown in Fig. 5a and c. The modeled potential temperature θ profiles consistently suggest the presence of the SBL, though the increasing of θ with height within the lowest 300 m is slightly smaller

170 than the measurements. The direction veering is well captured in the lowest 300 m. Above 300 m, the measurements suggest a persistent wind direction of about 250°, while the modeled wind vector continues turning an additional $10 - 20°$. LLJs are observed during these profiling flights, as shown in Fig. 5g; note that the time and location of these flights are different (Table 1 and Fig. 2). Fig. 5g clearly suggests that the wind structure of the LLJs is highly variant over time and space. This is also true with the modeled LLJs corresponding to these profiling flights, see Fig. 5g. Several of the measured wind speed profiles

175 have more than one jet nose, with the lowest ones beneath 200 m and the highest ones at $350 - 400$ m, suggesting the presence of multiple internal boundary layers in associated with the flow from the land. The model captures the jets at the level 300 $- 400$ m. At the same time, both measured and modeled TKE decrease generally with height, with the modeled values being larger, see Fig. 5e and f. While the mean TKE values from the measurements are relatively small, their fluctuations are two times larger. These are not shown here in order to avoid too much noise in the plot. As none of these profile-flight data are

180 affected by wind farm wakes, the modeled data are the same for NWF, the Fitch and the EWP schemes. Therefore, in Fig. 5, only results from the EWP scheme are shown.

   With the wind from the southwest direction, at the FINO 1 site, the LLJ structure is affected by the wake effect from upstream Borkum Riffgrund wind farm. Figure 6 shows the wind speed profiles at FINO 1 during three 1-h periods, with two during the flight periods (Fig. 6a and b) and one later in the afternoon (Fig. 6c). Six 10-min modeled data during one hour from three

185 simulation modes are plotted together with the 10-min measured data. The measurements only reach up to 100 m, which is way beneath the jet noses. The following characteristics can be observed from Fig. 6: (1) The Fitch scheme results in smaller wind reduction below upwind hub height but larger wind speed reduction between hub height up to the rotor top height than the EWP scheme. Thus the average values from the surface to the rotor top height are comparable between the two schemes. (2) The wind speed reduction is not limited to the rotor area, but up to the jet nose; (3) The position of the LLJ nose is higher

190 in the presence of the farm wake effect according to the WRF modeling; (4) There is a kink in the wind profile from the Fitch scheme, which is absent in the results from the EWP scheme. The measured profiles are closer to the EWP scheme for Fig. 6a and b when the jet nose is high, but they are in better agreement with the Fitch scheme for Fig. 6c when the jet nose is low.

These characteristics are also examined for another location, here point A as shown in Fig. 3. Point A is inside the Godewind 1 wind farm area and it is on top of the flight leg, transect-a. The transect-flight data at the closest time (number four in Table 1,

195   15:01 – 15:11), averaged over a distance of 2 km, are plotted on top of the profiles at $z =250$ m as star for wind speed (Fig. 7a) and TKE (Fig. 7b), where the corresponding wind speed and TKE from the three simulation modes are shown, respectively. The above descriptions of the wind speed for FINO1 are also true for point A, as can be seen in Fig. 7a. Here the EWP scheme provides a better estimate of mean wind speed. In the absence of wind farms (NWF), TKE decreases with height, as in Fig. 5. In the presence of farm wakes, with both schemes, TKE increases with height up to the rotor top height and then decreases

200   again to a value matching the free stream value. TKE from the Fitch scheme increases significantly with height, and for the value at point A, it is overestimated in comparison with the flight data. Over the rotor area, the variation of TKE with height from the EWP scheme is smoother and the magnitude of TKE significantly smaller in comparison with the Fitch scheme (Fig. 7b). There is considerable fluctuation of the measured TKE with time and space; the variation of the measured and modeled TKE along the flight track will be further analyzed in section 3.2.

205   ## 3.2 Wind farm wake effects

The vertical profile of wind speed at the FINO 1 site clearly shows the wake effect from the upstream Borkum Riffgrund wind farm. Figure 8 compares the measured and modeled time series of wind speed and wind direction at FINO 1. Here the modeled values at FINO 1 are weighted between two closest grid points (one inside and one outside the farm) according to the distances between the grid points and the mast location. This is done because the closest grid point to FINO 1 is inside

210   the farm, while in reality, FINO 1 is on the edge, and outside of the farm. The three model modes (NWF, Fitch, EWP) provide the same wind direction calculations at 90 m which follow the measurements well until late in the afternoon when the modeled winds are more westerly than in reality (Fig. 8b). The wake impact on the wind speed at 100 m is clear, as shown in Fig. 8a. Between 12:00-24:00 on 14 Oct, the difference between the measured and NWF-modeled mean wind speed, $\langle \Delta U \rangle = -1.41$ m s^{-1}, the standard deviation of the difference $STD = 0.56$ m s^{-1}, and the absolute difference $\langle |\Delta U| \rangle = 1.41$

215   m s^{-1}, respectively. Comparison between the measurements and the Fitch scheme gives $\langle \Delta U \rangle = 0.30$ m s^{-1}, $STD = 0.46$ m s^{-1} and $\langle |\Delta U| \rangle = 0.44$ m s^{-1}. Comparison between the measurements and EWP scheme gives $\langle \Delta U \rangle = -0.2$ m s^{-1}, $STD = 0.52$ m s^{-1} and $\langle |\Delta U| \rangle = 0.45$ m s^{-1}. This suggests that, during this period, the wake effect is on average about 1.71 m s^{-1} when calculated using the Fitch scheme and 1.21 m s^{-1} when calculated using the EWP scheme. Without taking wind farm wake into account, WRF overestimates the wind speed at 100 m by 1.41 m s^{-1}. The Fitch scheme overestimates and the

220   EWP scheme underestimates $\langle \Delta U \rangle$, with the EWP providing a slightly smaller bias.

The wind farm wakes are visible from the SAR image at 17:17 UTC from Fig. 1a. The corresponding 10-m wind speed from WRF using the Fitch and the EWP schemes are shown in Fig. 1b and c, respectively. Even though WRF misses detailed patterns as in the SAR image (e.g. streaks and waves), the farm wake patterns are consistent. Comparing the wind speeds in the wake shadows and the surrounding free stream, both SAR data and WRF output suggest a wind reduction of about $1.5 - 2$ m

225   s^{-1}, with the wind speeds in the farm wakes in the range of $7 - 8$ m s^{-1}, and the free stream wind speeds in the range of $9 - 10$ m s^{-1}. To make the wind farm wake effect more visible, the difference of the wind speed in Fig. 1b and c to the NWF is shown

as 10-m wind speed deficit in Fig. 9a (Fitch-NWF) and b (EWP-NWF), respectively. Here one can see that the wake-caused wind speed reduction at 10 m is about 2.5 ms^{-1} inside the farm and a reduction of 0.5 ms^{-1} can extend between ten and a hundred of kilometers downwind, superimposing with wakes from other wind farms. At 17:17, the SAR 10-m wind speed at the FINO 1 site is about 8 m s^{-1}, and the WRF outputs, both from the Fitch and the EWP schemes, are also about 8 m s^{-1}. Note that in a short distance downwind of the wind farms, the surface wind at 10 m from the Fitch scheme suggests a slight speedup, see the brighter color in the farm wake shadows in Fig. 1b and the white color in Fig. 9a. This is a phenomenon that deserves further investigation (Djath et al., 2018), but it is beyond the scope of this study.

The transect-flight data over transect-a are plotted in Fig. 10a and b for wind speed and TKE, respectively. There are altogether six flights over transect-a between approximately 14:20 and 16:10 (Table 1), each lasted approximately 10 minutes. The flight data are at 250 m above sea level, averaged here over a spatial distance of both 2 km (same as the WRF spatial resolution) and 1.5 km (same as in S2020). The results of using the two averaging distances are similar; the one using 1.5 km provides slightly more fluctuation. Here we only show the results using 2 km. The corresponding model data at 250 m over transect-red in Fig. 3 from 14:00 to 16:00, covering the flight periods, are plotted (Fitch, EWP and NWF). The modeled data are 10-min instantaneous values, plotted every half an hour. Compared to the ambient flow, there is a deficit in wind speed at 250 m above the wind farm Godewind 1, due to the wind farm effects. Such a wind deficit is almost 3 m s^{-1} in the flight data, and it is also about 3 m s^{-1} in the modeled data using the Fitch scheme, but only about 2 m s^{-1} in the modeled data using the EWP scheme.

As a result of the wind farm parameterizations, above the wind farm high TKE values are observed when compared with ambient values, which are almost zero (Fig. 10b). When no wind farms are included in the modeling, there is no systematic difference in TKE across transect-a, see the black curves. Parametrizations of the wind farms result in increased TKE over the farm. At 250 m, the Fitch scheme provides TKE inside the range of the measured values, though with large underestimation at the southern edge of the farm and with comparable magnitude at the northern edge of the farm. The profiles at point A (Fig. 7b), which is approximately in the center of transect-a and transect-red (Fig. 3), show that the TKE values are highest close to hub height and decrease above it. At point A, the TKE value simulated by the Fitch scheme is about 2.3 m^2 s^{-2} at rotor top height, which is about 40% higher than that at 250 m. For transect-a, the TKE values from the EWP scheme are considerably smaller, being only about 1/4 of the values from the Fitch scheme, and are thus significantly underestimated compared to the flight measurements.

One can notice the speedup in the flow in the flight measurements on the southern edge of the farm in Fig. 10a, as also pointed out in S2020; see the bump of wind speed at 250 m at latitude before 54°N. WRF does not capture this phenomenon with either scheme. The abrupt increase in TKE in the same area (Fig. 10b) is likely related to this flow acceleration and is also missing in the WRF results.

The vertical distributions of the wind speed and TKE along transect-a are shown in contour lines in Fig. 11 (latitude versus height) for 15:30 for both Fitch and EWP, as an example. The LLJs are visible here in Fig. 11 with the wind speed maximum height between ~300 and 500 m. The largest difference in the wind speed between the Fitch and EWP schemes is over the

farm beneath the rotor top, with Fitch simulating on average larger wind speed reductions from the wind farm wake effect (Fig. 11a and b).

Fig. 11c and d show that, the largest TKE values are located at a height between hub height and rotor top with the Fitch scheme, and they are located closer to the rotor top with the EWP scheme. The Fitch scheme simulates several times larger

265   TKE values than the EWP scheme, with the largest difference over the wind farm area. An increase in TKE is notable up to double the height of the rotor top. Outside the farm area and even in the wake region, the two schemes provide similar wind speed and TKE values. This can for example be seen in Fig. 12, which is for the transect-blue as in Fig. 3b (longitude approximately 7.2°E). These characteristics can also be seen in a bird view of the spatial distribution of TKE at 250 m over the wind farm cluster with the Godewind 1 farm in the domain center, shown in Fig. 13a and b, for the Fitch and the EWP scheme,

270   respectively, for the same time as in Figs. 11 and 12.

4   Discussion

For the first time, the calculations of both wind speed and TKE from two explicit wind farm parametrization schemes (Fitch and EWP) in WRF are compared and verified through a case study, thanks to the open access high frequency flight data over and around the wind farm Godewind 1 (Bärfuss et al., 2019a) and FINO 1 measurements. This study thus complements S2020

275   where only the Fitch scheme was used to model the wind farm wake.

The farm wake effect is observed in a variety of measurements: in the FINO 1 mast measurements shown as vertical wind-profile and time series, in the SAR 10-m wind speed shown as spatial distribution and in the flight data shown as cross-wind farm transect distribution of wind speed and TKE at 250 m. The WRF modeling with the two farm parametrization schemes captures these observed farm wake effect consistently in terms of wind speed, but with some noticeable differences. In the

280   vertical wind-profiles at FINO1, when compared to the EWP scheme, the wind speed deficit due to the wind farm wakes using the Fitch scheme is more centered and more pronounced around the hub height and rotor area, shown as a kink. In the EWP scheme, due to the subgrid-scale vertical wake expansion, the wind deficit is more spread and smooth over the rotor area. The larger wind speed deficit in association with the Fitch scheme beneath the rotor top height is also visible over the wind farm and in the wake areas. The flight data suggests a flow acceleration on the southern side of the wind farm Godewind 1

285   accompanying the flow from the southwest. This acceleration is however not captured in WRF. It is expected that a high fidelity model is needed to resolve this feature.

Even though the modeled wind speeds are comparable using the two schemes, the results on TKE are significantly different. The Fitch scheme, having TKE contributions from both the shear and an explicit term related to the turbine power and thrust coefficients, provides TKE values several times larger than those from the EWP scheme over the wind farm. In addition, WRF

290   misses the flow acceleration south to the farm and it underestimates TKE in the adjacent wind farm area. At the northern part of the farm, the modeled TKE values using the Fitch scheme are of comparable magnitudes with respect to to the measurements. TKE values from the EWP scheme are significantly underestimated. This suggests that turbine-induced TKE does not only develop from the shear, as assumed in the EWP scheme, but instead an explicit source is required. The difference in the

TKE magnitude from the two schemes become quickly negligible away from the farm area, likely due to the fact that the
295   TKE-advection is not activated in the simulation using the Fitch scheme (Section 2.2).

This is not the case when the wind-farm-induced TKE-advection scheme is turned on, as shown in the spatial distribution
of TKE over farm-cluster around the Godewind 1 with a farm-induced TKE factor C_{TKE} =0.25 and 1 in Fig. 13c and d,
respectively. Unlike in Fig. 13a, where farm-induced TKE is mostly above the wind farm, it is advected in the mean wind
direction in Fig. 13c and d. TKE in the EWP scheme, as a function of the wind shear, follows the mean flow. The spatial
300   gradient patterns of TKE are more similar between the two schemes, comparing 13b with c and d. In addition, model results
with C_{TKE} =0.25 and 1 are also used to compare with the mean wind speed and TKE at 250 m from the flight track, in
the same way as in Fig. 10, which are shown in Fig. 14. It remains inconclusive how much the inclusion of farm-induced-
TKE advection improves the results and what are the correct C_{TKE} values to use; more measurements are needed for further
investigation.

305   The studied case becomes even more interesting due to the presence of LLJs, in addition to the wind farm effect, as LLJ
is a common phenomenon in this area of the North Sea. Numerical modeling studies of wind energy usually address the rich
resource in connection with LLJs, though few have included wind farm wake effect. This case study shows an overestimation
of the 100-m wind speed by 1.59 m s^{-1} when ignoring the wind farm effect in the WRF modeling, accounting 13−22% of
the mean wind speed during this simulation period. At the same time, measurements and modeling at FINO 1 suggest that the
310   wind speed distribution with height in the presence of LLJ is modified by the presence of wind farm wakes, showing a higher
jet nose and a higher wind shear beneath the jet nose. This upward shift of the jet nose in the presence of a wind farm was also
modelled in different LES studies (Sharma et al., 2017; Abkar et al., 2016).

5   Conclusions

It is important to take the wind farm wake effect into account when calculating LLJ wind speeds in areas with wind farms.
315   LLJ structures are affected by the presence of wind farms. The WRF model with both the Fitch and the EWP schemes can
capture the wind speed field rather well and consistently. The schemes can not capture the flow acceleration along the farm
edge. TKE from the EWP scheme is significantly underestimated compared to the flight measurements. This suggests that an
explicit turbine-induced source of TKE should be included in addition to the shear-generated TKE.

This case study shows typical features of the wind farm wakes in the presence of LLJs through a few key parameters,
320   using the most-used modeling approaches. It raises issues that have not been addressed in the literature, namely the interaction
of wind farm wakes and LLJs. It also clearly shows the need in the improvement of TKE calculations using the wind farm
parameterizations in WRF. This study therefore serves as a start for a more systematic study of similar conditions.

Code and data availability.   The WRF model code is publicly available at http://www2.mmm.ucar.edu/wrf/users/downloads.html. The WRF
configuration files and files for using the wind farm parameterizations of Fitch et al. (2012) as well as Volker et al. (2015) are available

325 at https://zenodo.org/record/4133350.X5aZOO3cBaR (DOI 10.5281/zenodo.4133350). The EWP codes are from those shared by Volker et al. (2015). The SAR data are available from https://satwinds.windenergy.dtu.dk/. The FINO 1 measurements can be assessed from http://fino.bsh.de/. The flight data are available on https://doi.org/10.1594/PANGAEA.902845. The OSTIA data is available from http://my.cmems-du.eu/motu-web/Motu. ERA5 data was downloaded from https://doi.org/10.24381/cds.bd0915c6. Data required for reproducing the model output in this study are shared on Zenodo at https://zenodo.org/record/4322866.X9iw2bNCfmE with DOI 10.5281/zen-
330 odo.4322866.

.

Author contributions. XL outlined the manuscript. XL and JF ran the simulations, performed the data analysis and wrote the draft.

Competing interests. The authors declare that they have no conflict of interest.

Acknowledgements. This study is supported by the ForskEL/EUDP OffshoreWake project (PSO-12521/EUDP 64017-0017). We thank the
335 open source platform https://doi.pangaea.de/10.1594/PANGAEA.902845 for the flight data and FINO 1 station. The satellite data in Fig. 1a is from https://satwinds.windenergy.dtu.dk/. We thank our colleagues Jake Badger, Andrea Hahmann and Rogier Floors for discussions. ERA5 data are downloaded from ECWMF and Copernicus Climate Change Service Climate Data Store. Data processing and visualization for this study was in part made using the python programming language and involved use of the following software packages: NumPy (van der Walt et al., 2011), pandas (McKinney, 2010), xarray (Hoyer and Hamman, 2017), Matplotlib (Hunter, 2007). The authors are grateful for
340 the tools provided by the open-source community.

References

Abkar, M., Sharifi, A., and Porté-Agel, F.: Wake flow in a wind farm during a diurnal cycle, Journal of Turbulence, 17, 420–441, https://doi.org/10.1080/14685248.2015.1127379, https://doi.org/10.1080/14685248.2015.1127379, 2016.

Archer, C. L., Wu, S., and Ma, Y.: Two corrections for turbulent kinetic energy generated by wind farms in the WRF model, Monthly Weather
345   Review, DOI 10.1175/MWR-D-20-0097.1, 2020.

Bärfuss, K., Hankers, R., Bitter, M., Feuerle, T., Schulz, H., Rausch, T., Platis, A., Bange, J., and Lampert, A.: In-situ airborne measurements of atmospheric and sea surface parameters related to offshore wind parks in the German Bight, https://doi.org/10.1594/PANGAEA.902845, https://doi.org/10.1594/PANGAEA.902845, 2019a.

Bärfuss, K., Hankers, R., Bitter, M., Feuerle, T., Schulz, H., Rausch, T., Platis, A., Bange, J., and Lampert, A.: In-situ airborne mea-
350   surements of atmospheric and sea surface parameters related to offshore wind parks in the German Bight, Flight 20171014_flight39, PANGAEA, https://doi.org/10.1594/PANGAEA.903088, https://doi.org/10.1594/PANGAEA.903088, in: Bärfuss, K et al. (2019): In-situ airborne measurements of atmospheric and sea surface parameters related to offshore wind parks in the German Bight. PANGAEA, https://doi.org/10.1594/PANGAEA.902845, 2019b.

Bundesnetzagentur: Turbines positions, $https://www.bundesnetzagentur.de/SharedDocs/Downloads$
355    $/DE/Sachgebiete/Energie/Unternehmen_Institutionen/ErneuerbareEnergien/ZahlenDatenInformationen$ $/VOeFF\_Registerdaten/2019\_01\_Veroeff\_RegDaten.html$, 2019.

Catton, M.: Climatological study of wakes from offshore wind farm clusters, Tech. Rep. DTU Wind Energy-M-0361, Wind Energy Department, DTU, Roskilde, Denmark, http://production.datastore.cvt.dk/oafilestore?oid=5f23fcaed9001d016b4e226dtargetid=5f23fcaed9001d016b4e2270, 2020.

360   Djath, B., Schulz-Stellenfleth, J., and Canadillas, B.: Impact of atmospheric stability on X-band and C-band synthetic aperture radar imagery of offshore windpark wakes, Journal of Renewable and Sustainable Energy, 10, 043 301, 2018.

Emodnet: Wind Farms (Polygons), $https://www.emodnet-humanactivities.eu/search-results.php?dataname=Wind+$ $Farms+(Polygons)$, 2020.

Energistyrelsen: Turbines positions, $https://ens.dk/service/statistik-data-noegletal-og-kort/data-oversigt-over-$
365    $energisektoren$, 2020.

Fischereit, J., Brown, R., Larsén, X. G., Badger, J., and Hawkes, G.: Review of mesoscale wind farm parameterisations and their applications, Boundary-Layer Meteorol., submitted, 2020.

Fitch, A. C., Olson, J. B., Lundquist, J. K., Dudhia, J., Gupta, A. K., Michalakes, J., and Barstad, I.: Local and Mesoscale Impacts of Wind Farms as Parameterized in a Mesoscale NWP Model, Monthly Weather Review, 140, 3017–3038, https://doi.org/10.1175/MWR-D-11-
370   00352.1, 2012.

Hersbach, H., Stoffelen, A., and de Haan, S.: An improved C-band scatterometer ocean geographical model function: CMOD5, J. Geophys. Res., 112, doi:10.1029/2006JC003 743, 2007.

Hoyer, S. and Hamman, J.: xarray: N-D labeled Arrays and Datasets in Python, Journal of Open Research Software, 5, 10, https://doi.org/10.5334/jors.148, 2017.

375   Hunter, J. D.: Matplotlib: A 2D Graphics Environment, Computing in Science Engineering, 9, 90–95, https://doi.org/10.1109/MCSE.2007.55, 2007.

Iacono, M. J., Delamere, J. S., Mlawer, E. J., Shephard, M. W., Clough, S. A., and Collins, W. D.: Radiative forcing by long-lived greenhouse gases: Calculations with the AER radiative transfer models, Journal of Geophysical Research, 113, 13 013, 2008.

Kain, J. S. and Fritsch, J. M.: Convective parameterization for mesoscale models: The Kain-Fritsch scheme. The representation of cumulus
380 convection in numerical models, Meteor. Monogr., Ameri. Meteor. Soc., 24, 165–170, 1993.

Kalverla, P., Steeneveld, G.-J., Ronda, R., and Holtslag, A. A. M.: Evaluation of three mainstream numerical weather prediction models with observations from meteorological mast IJmuiden at the North Sea, Wind Energy, 22, 34–48, https://doi.org/10.1002/we.2267, 2019.

Lampert, A., Bärfuss, K., Platis, A., Siedersleben, S., Djath, B., Cañadillas, B., Hankers, R., Bitter, M., Feuerle, T., Schulz, H., Rausch, T., Angermann, M., Schwithal, A., Bange, J., Schulz-Stellenfleth, J., Neumann, T., and Emeis, S.: In-situ airborne measurements of
385 atmospheric and sea surface parameters related to offshore wind parks in the German Bight, https://doi.org/10.1594/PANGAEA.902845, https://doi.org/10.1594/PANGAEA.902845,.

Langor, E. N.: Characteristics of Offshore Wind Farm Wakes and their Impact on Wind Power Production from Long-term Modelling and Measurements, Tech. Rep. DTU Wind Energy-M-0315, 2019.

Lee, J. C. and Lundquist, J. K.: Evaluation of the wind farm parameterization in the Weather Research and Forecasting model (version 3.8.1)
390 with meteorological and turbine power data, Geoscientific Model Development, 10, https://doi.org/10.5194/gmd-10-4229-2017, 2017a.

Lee, J. C. and Lundquist, J. K.: Observing and Simulating Wind-Turbine Wakes During the Evening Transition, Boundary-Layer Meteorology, 164, 449–474, https://doi.org/10.1007/s10546-017-0257-y, 2017b.

McKinney, W.: Data Structures for Statistical Computing in Python, in: Proceedings of the 9th Python in Science Conference, edited by van der Walt, S. and Millman, J., https://conference.scipy.org/proceedings/scipy2010/pdfs/mckinney.pdf, last access: 27 October 2020,
395 2010.

Nakanishi, M. and Niino, H.: Development of an improved turbulence closure model for the atmospheric boundary layer, J. Meteorol. Soc. Jpn, 87, 895–912, 2009.

Nunalee, C. G. and Basu, S.: Mesoscale modeling of coastal low-level jets: implications for offshore wind resource estimation, Wind Energy, 17, 1199–1216, 2014.

400 Platis, A., Siedersleben, S. K., Bange, J., Lampert, A., Bärfuss, K., Hankers, R., Cañadillas, B., Foreman, R., Schulz-Stellenfleth, J., Djath, B., Neumann, T., and Emeis, S.: First in situ evidence of wakes in the far field behind offshore wind farms, Scientific Reports, 8, https://doi.org/10.1038/s41598-018-20389-y, 2018.

Pryor, S. C., Shepherd, T. J., Volker, P. J. H., Hahmann, A. N., and Barthelmie, R. J.: "Wind Theft" from Onshore Wind Turbine Arrays: Sensitivity to Wind Farm Parameterization and Resolution, Journal of Applied Meteorology and Climatology, 59, 153–174,
405 https://doi.org/10.1175/jamc-d-19-0235.1, {%}3CGoto, 2020.

Sharma, V., Parlange, M. B., and Calaf, M.: Perturbations to the Spatial and Temporal Characteristics of the Diurnally-Varying Atmospheric Boundary Layer Due to an Extensive Wind Farm, Boundary-layer Meteorology, 162, 255–282, https://doi.org/10.1007/s10546-016-0195-0, 2017.

Shepherd, T. J., Barthelmie, R. J., and Pryor, S. C.: Sensitivity of Wind Turbine Array Downstream Effects to the Parameterization Used
410 in WRF, Journal of Applied Meteorology and Climatology, 59, 333–361, https://doi.org/10.1175/JAMC-D-19-0135.1, http://journals.ametsoc.org/doi/10.1175/JAMC-D-19-0135.1, 2020.

Siedersleben, S. K., Platis, A., Lundquist, J. K., Djath, B., Lampert, A., Bärfuss, K., Canadillas, B., Schulz-Stellenfleth, J., Bange, J., Neumann, T., and Emeis, S.: Observed and simulated turbulent kinetic energy (WRF 3.8.1) over large offshore wind farms, Geoscientific Model Development, 13, 249–268, https://doi.org/http://doi.org/10.5194/gmd-2019-100, 2020.

415 Skamarock, W., Klemp, J., Dudhia, J., Gill, D., Barker, D., Wang, W., and Powers, J.: A Description of Advanced Research WRF, Tech. Rep.
        NCAR/TN-468+STR, NCAR, NCAR, Boulder, Colorado, USA, 2007.

Smedman, A.-S., Tjernström, M., and Högström, U.: Analysis of the turbulence structure of a marine low-level jet, Boundary-Layer Meteorol,
        66, 105–126, 1993.

Smedman, A.-S., Bergström, H., and Högström, U.: Spectra, variance and length scales in a marine stable boundary layer dominated by a
420   low level jet, Boundary-Layer Meteorol, 76, 211–232, 1995.

Stark, J. D., Donlon, C. J., Martin, M. J., and McCulloch, M. E.: OSTIA : An operational, high resolution, real time, global sea surface
        temperature analysis system, in: Oceans '07 IEEE Aberdeen, conference proceedings. Marine challenges: coastline to deep sea, Aberdeen,
        Scotland, 2007.

Tay, K., Koh, T., and Skote, M.: Characterizing mesoscale variability in low-level jet simulations for CBLAST-LOW 2001 campaign, Mete-
425   orology and Atmospheric Physics, https://doi.org/https://doi.org/10.1007/s00703-020-00736-3, 2020.

Tennekes, H. and Lumley, J. L.: A first course in turbulence, The MIT Press, 1972.

Thompson, G., Rasmussen, R. M., and Manning, K.: Explicit forecasts of winter precipitation using an improved bulk microphysics scheme.
        Part-I: Description and sensitivity analysis, Mon. Weather Rev., 132, 519–542, 2004.

Tomaszewski, J. M. and Lundquist, J. K.: Simulated wind farm wake sensitivity to configuration choices in the Weather Research and
430   Forecasting model version 3.8.1, Geoscientific Model Development, 13, 2645–2662, https://doi.org/10.5194/gmd-13-2645-2020, 2020.

Valenzuela, G.: Theories for the interaction of electromagnetic and ocean waves - A review, Boundary-Layer Meteorol, 13, 61–85, 1978.

van der Walt, S., Colbert, S. C., and Varoquaux, G.: The NumPy Array: A Structure for Efficient Numerical Computation, Computing in
        Science Engineering, 13, 22–30, https://doi.org/10.1109/MCSE.2011.37, 2011.

Volker, P. J. H., Hahmann, A. N., Badger, J., and Jørgensen, H. E.: Prospects for generating electricity by large onshore and offshore wind
435   farms, Environmental Research Letters, https://doi.org/10.1088/1748-9326/aa5d86, https://doi.org/10.1088/1748-9326/aa5d86,volume=
        {12},year={2017}.

Volker, P. J. H., Badger, J., Hahmann, A. N., and Ott, S.: The Explicit Wake Parametrisation V1.0: a wind farm parametrisation in the
        mesoscale model WRF, Geoscientific Model Development, 8, 3715–3731, https://doi.org/10.5194/gmd-8-3715-2015, 2015.

Wagner, D., Steifeld, G., Witha, B., Wurps, H., and Reuder, J.: Low Level Jets over the Southern North Sea, Meteorol. Z., 28, 389–415, 2019.
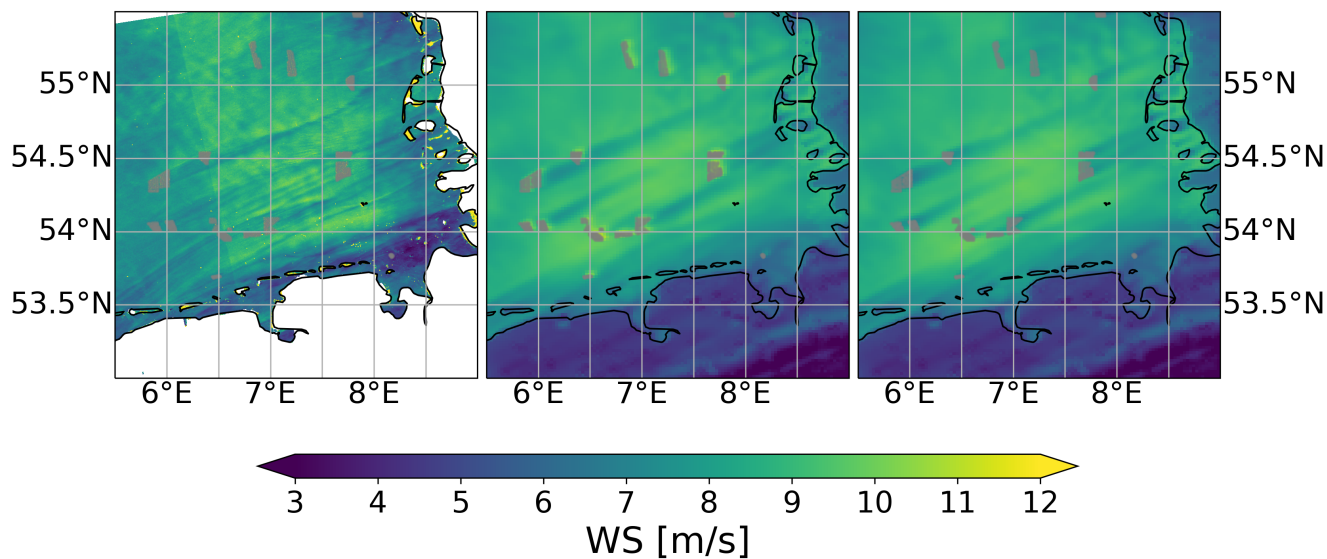
Figure 1. Wind speed (ms^{-1}) at about 10 m (a) From SAR at 17:17 UTC on 14 Oct 2017; (b) from WRF with the Fitch scheme at 17:10; (c) from WRF with the EWP scheme at 17:10 on 14 Oct. The satellite data in (a) are taken from https://satwinds.windenergy.dtu.dk/.
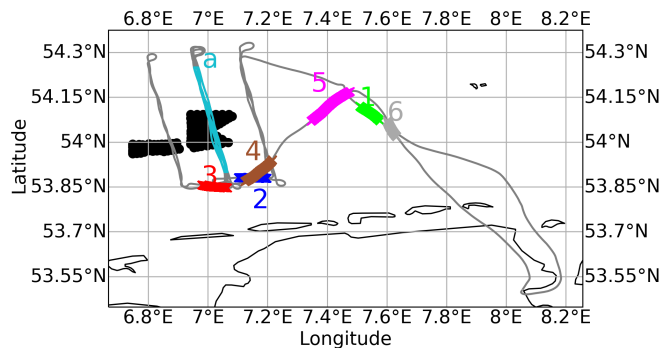
Figure 2. Flight tracks on 14 Oct 2017. Track labeled with "a" provides transect-flight data over the wind farm at about 250 m. Tracks labeled with numbers 1 to 6 provide the profile-flight data (see also Table 1). The flight track has been extracted from Bärfuss et al. (2019b).
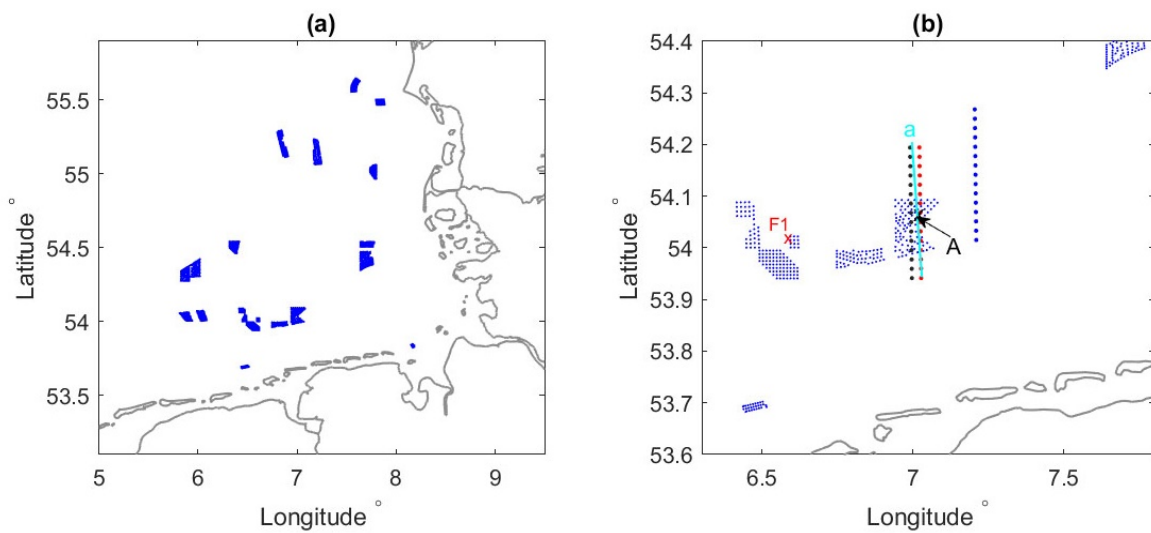
Figure 3. (a). Wind farm clusters that are included in the WRF modeling. (b). Close-up of (a), where the two consecutive rows over the Godewind 1 farm are WRF grid points (black and red), the flight legs are in between the two row of WRF grid points (transect labeled "a" in cyan as in Fig. 2) and one more row down wind (blue). Also marked are the location of the FINO 1 mast (F1) and point A on transect-a.
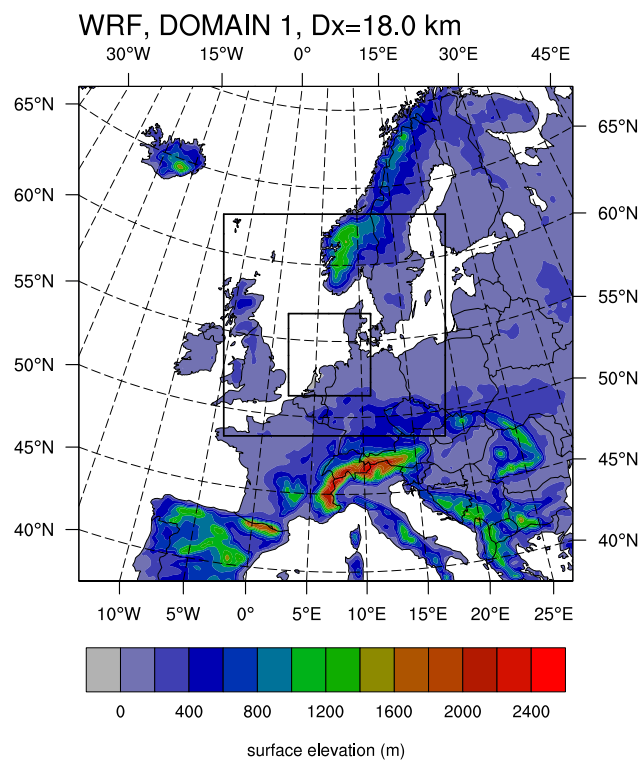
Figure 4. The three nested model domains in the WRF modeling, shown in topography.
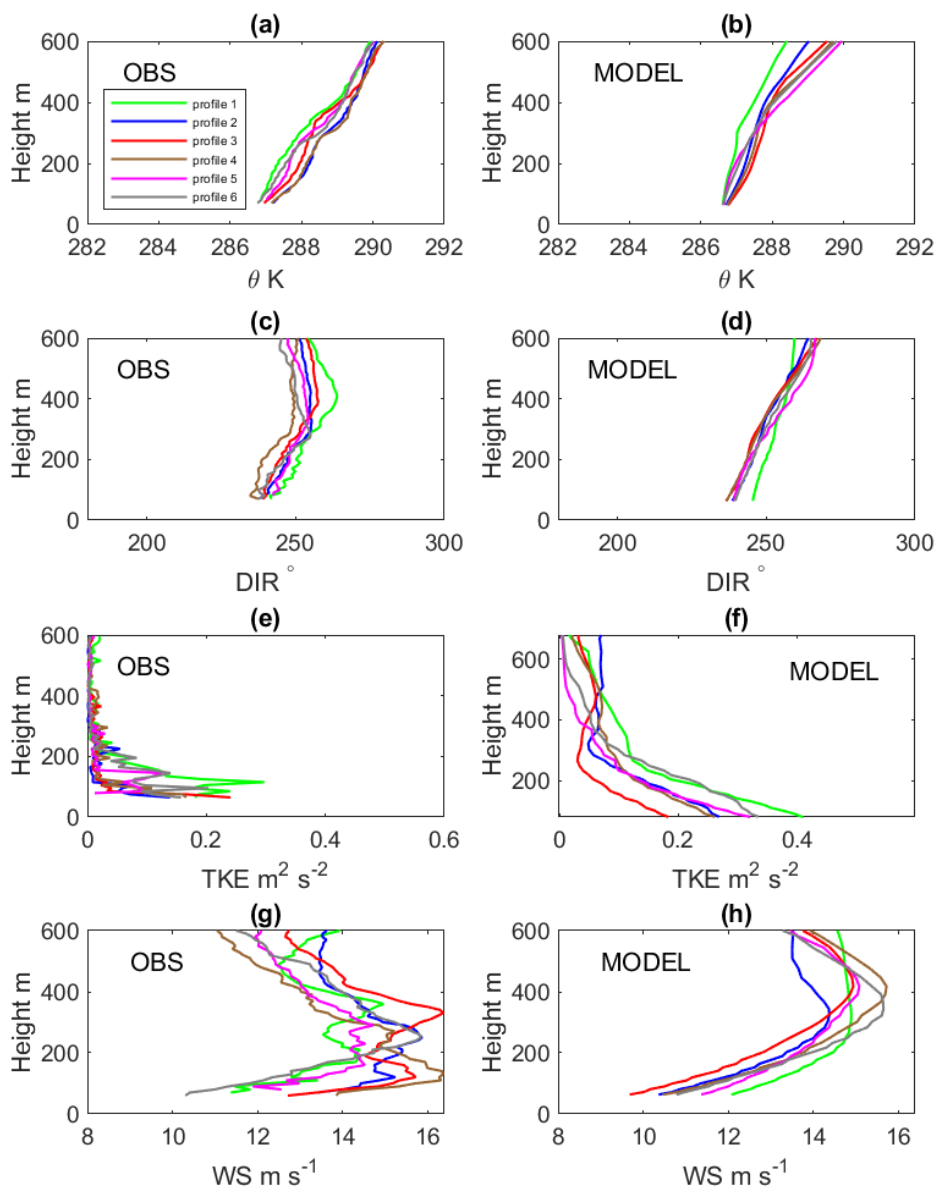
Figure 5. Vertical profiles of potential temperature (a, b), wind direction (c, d), TKE (e, f) and wind speed (g, h), observed (OBS) and modeled (MODEL) at the center positions of profile-flight 1 to 6. Note that the modeled data are from EWP scheme.
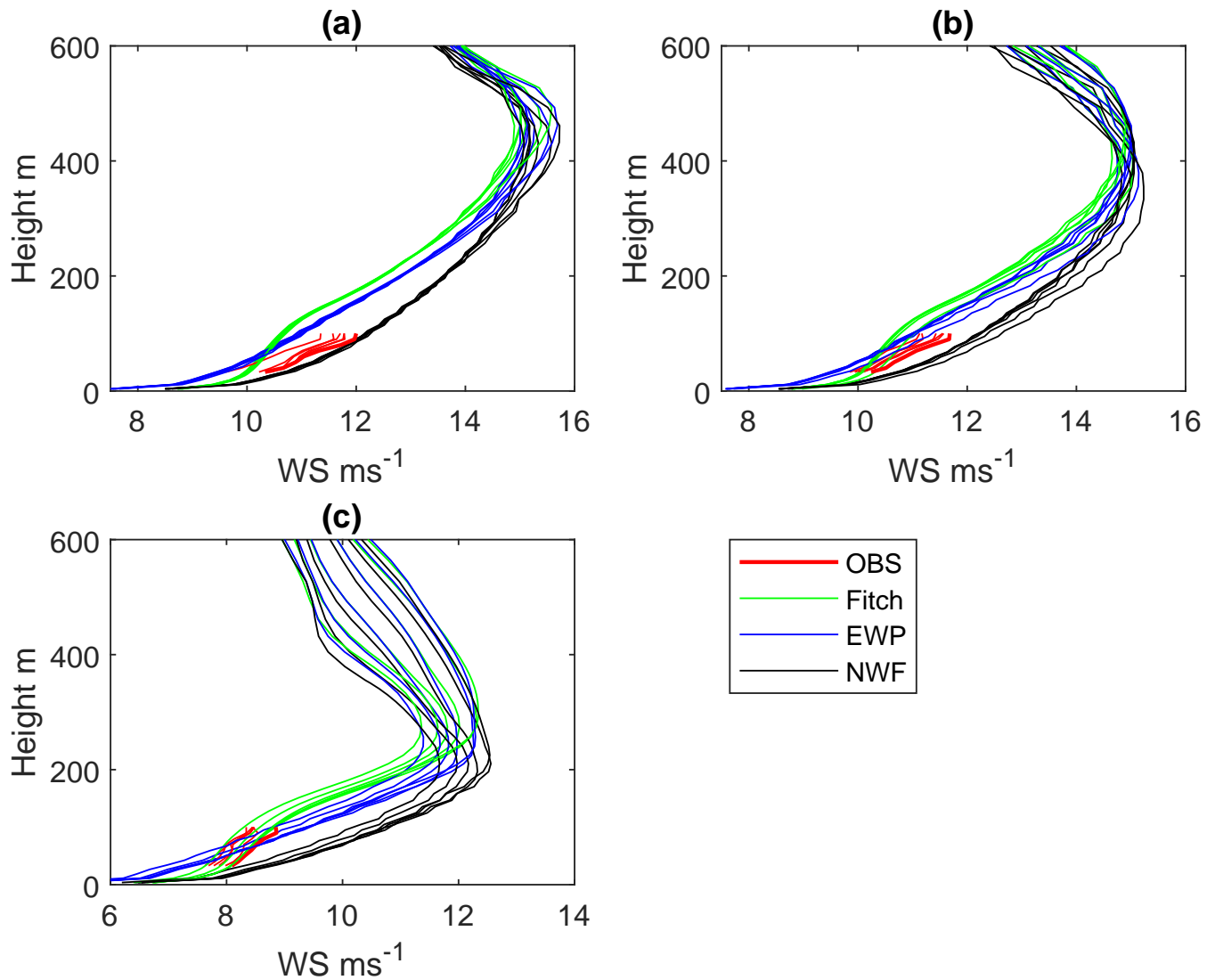
Figure 6. Wind profiles measured (OBS) and modeled (Fitch, EWP and NWF) at FINO 1 station on 14 Oct. (a) six 10-min profiles between 14:00 and 15:00; (b) six 10-min profiles from 15:00-16:00; (c) six 10-min profiles from 20:00-21:00.
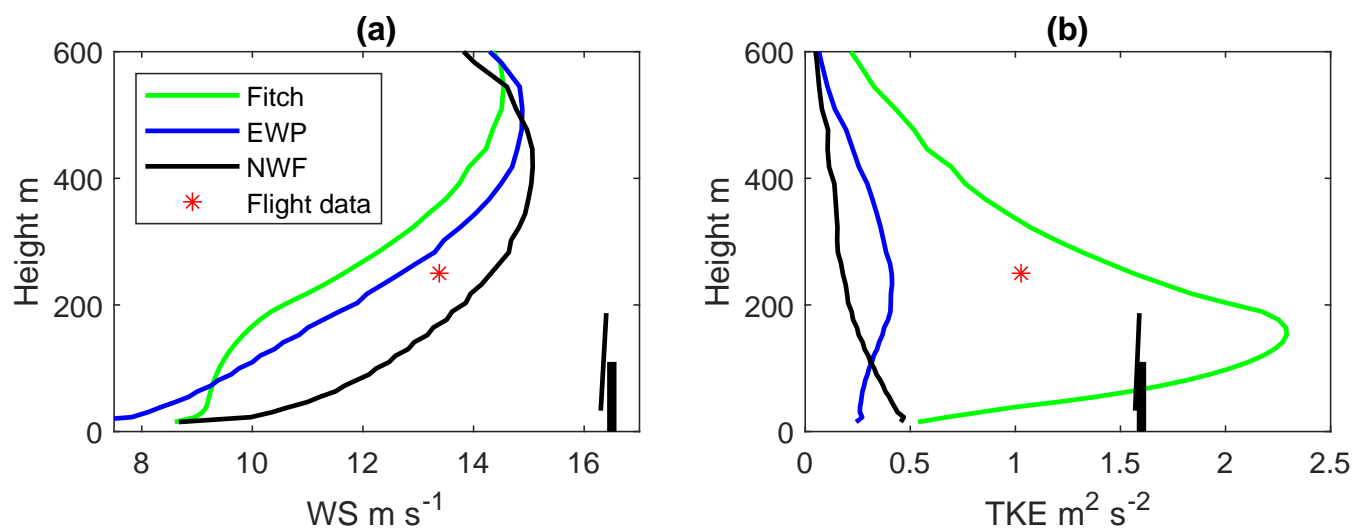
Figure 7. Modeled vertical profiles at Point A (see Fig. 3) over the Godewind 1 wind farm at 15:00 on 14 Oct, together with the transect-flight-4 data at 250 m (15:01 - 15:11) (a) wind speed; (b) TKE. The corresponding turbine hub height and the rotor area are illustrated in gray.
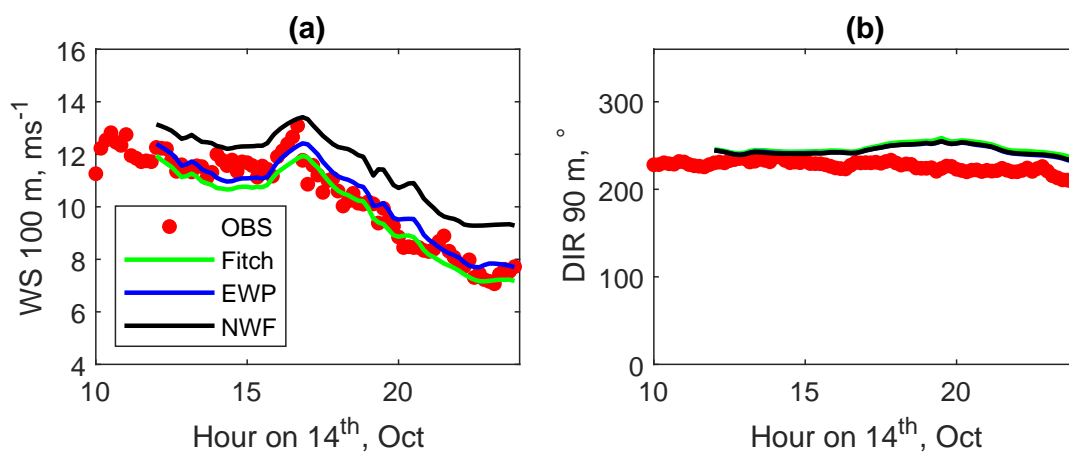
Figure 8. Measured and modeled time series at FINO 1 on the 14 Oct 2017: (a) wind speed at 100 m; (b) wind direction at 90 m, using Fitch and EWP schemes, as well as no farms option (NWF).
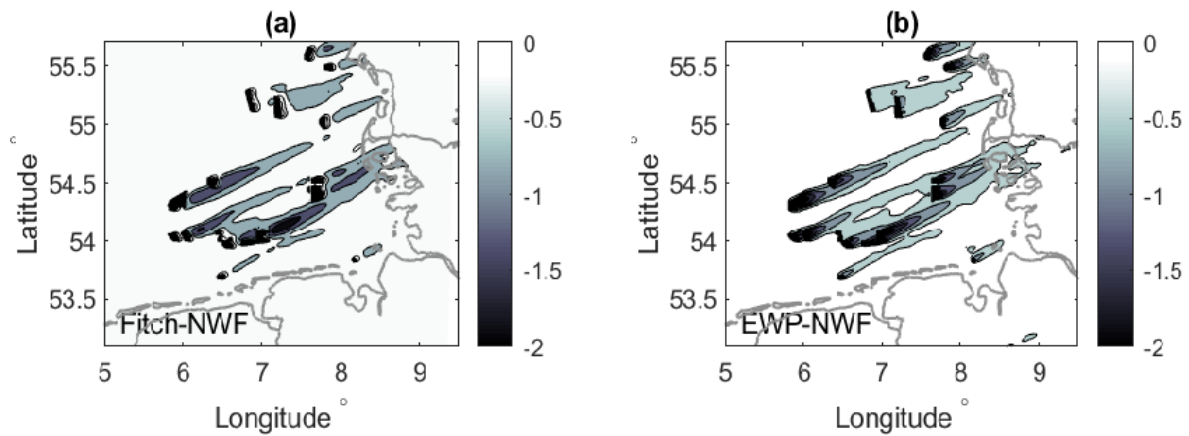
Figure 9. Wind speed deficit (m s^{-1}) at about 10 m 17:00 on 14 Oct 2017, corresponding to the SAR image as in Fig. 1. (a) wind speed from the Fitch scheme minus those from the no-farm scheme (Fitch-NWF) (b) wind speed from the EWP scheme minus those from the no-farm scheme (EWP-NWF).
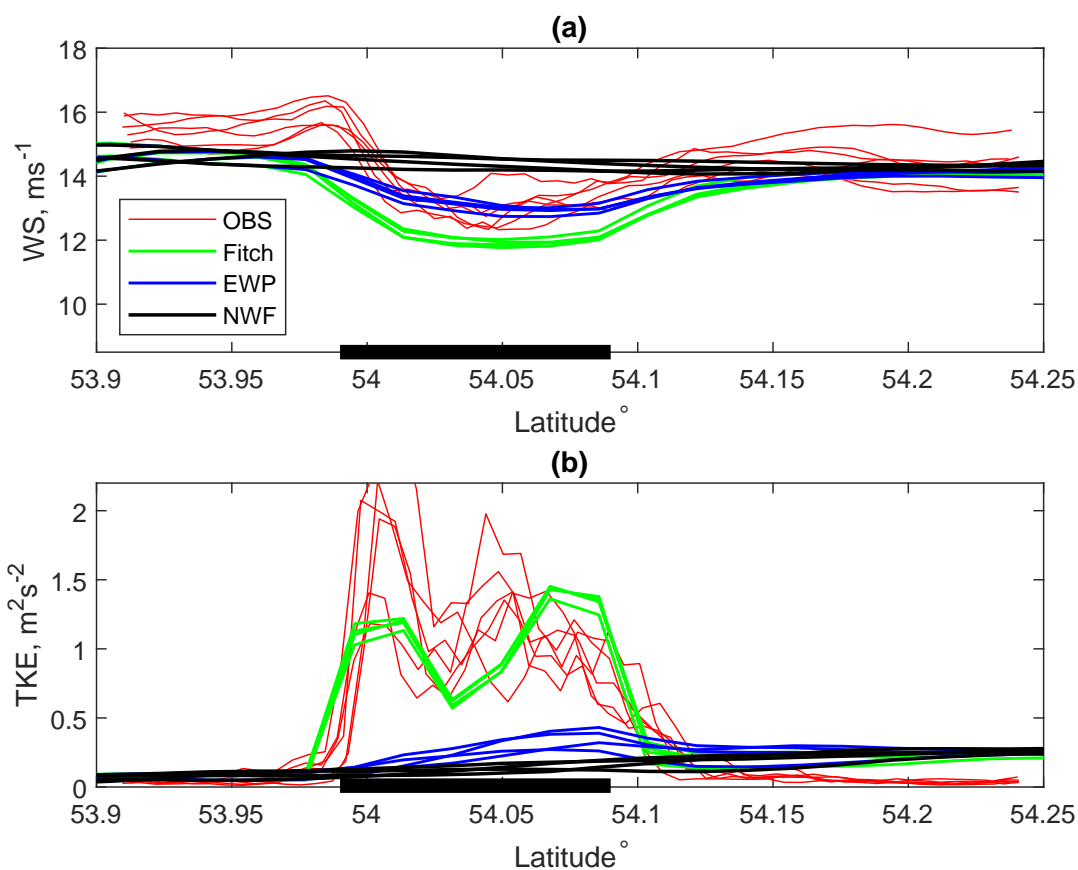
Figure 10. (a) Transect distribution of wind speed at 250 m as a function of latitude between 14:00 to 16:00 on 14 Oct 2017, observed (OBS) and modeled (every 30-min). (b) Similar to (a) but for TKE. The observed values are the flight data averaged over a distance of 2 km. The modeled values are from the use of the Fitch, the EWP and no wind farm (NWF) schemes. The wind farm is indicated on the $x-$axis with a thick black line.
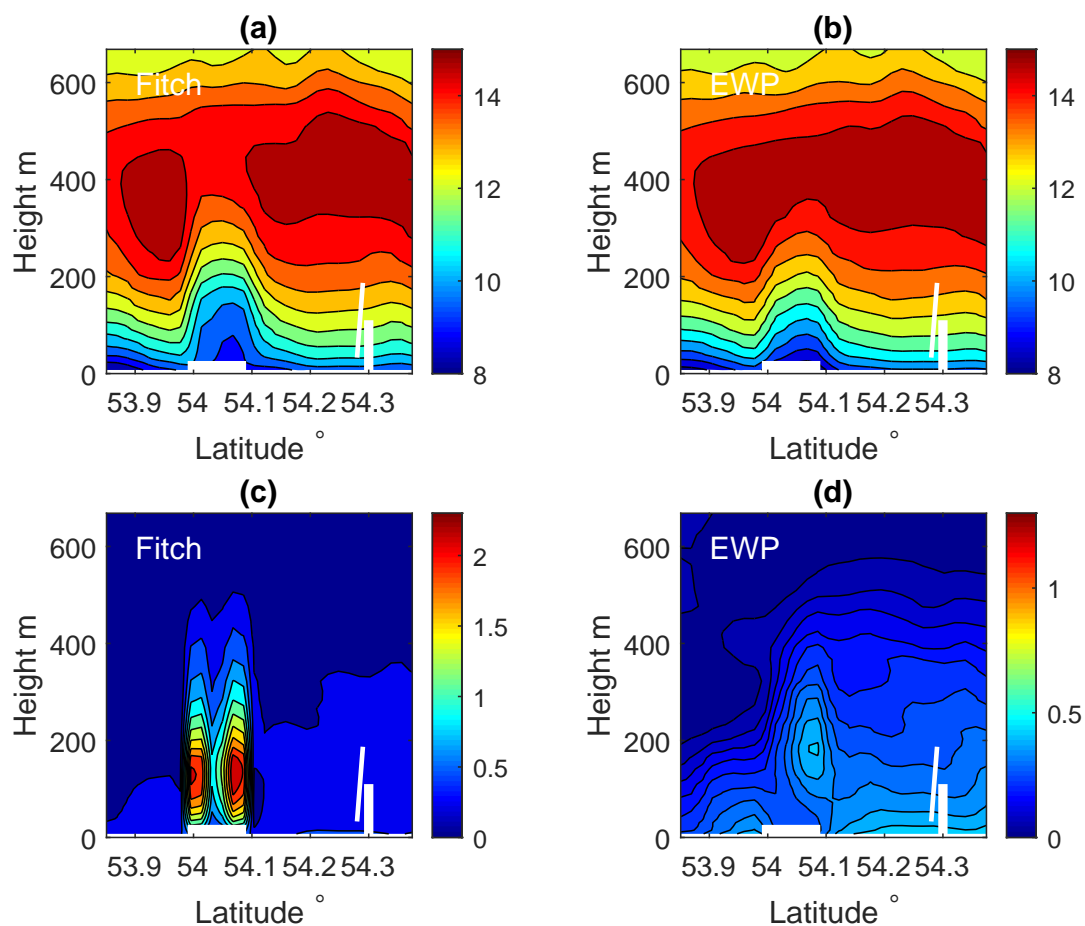
Figure 11. Distribution of wind speed and TKE over the transect-red (at longitude 7.02°E) at 15:30 on 14 Oct 2017 The wind farm is indicated on the $x-$axis with a thick white line and the corresponding turbine is illustrated in white.
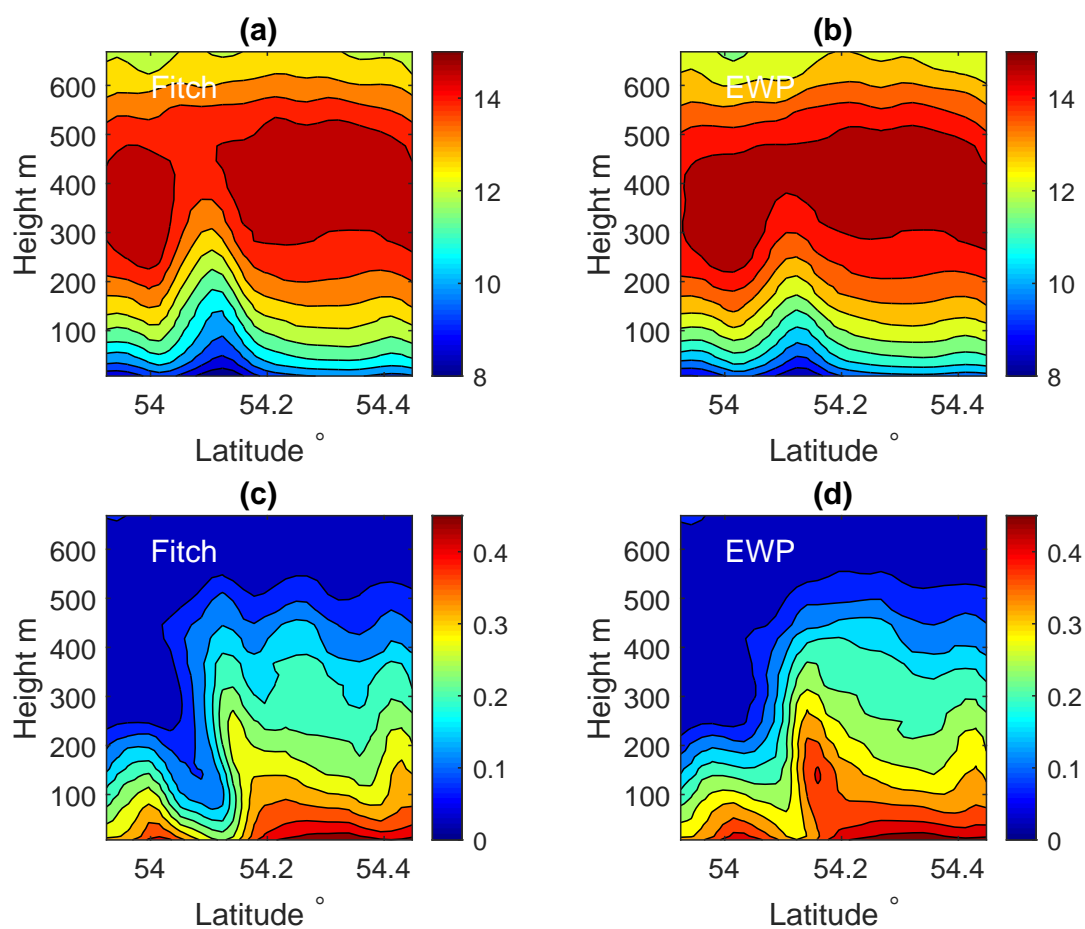
Figure 12. Distribution of wind speed and TKE over the transect-blue (at longitude 7.2°E) at 15:30 on 14 Oct.
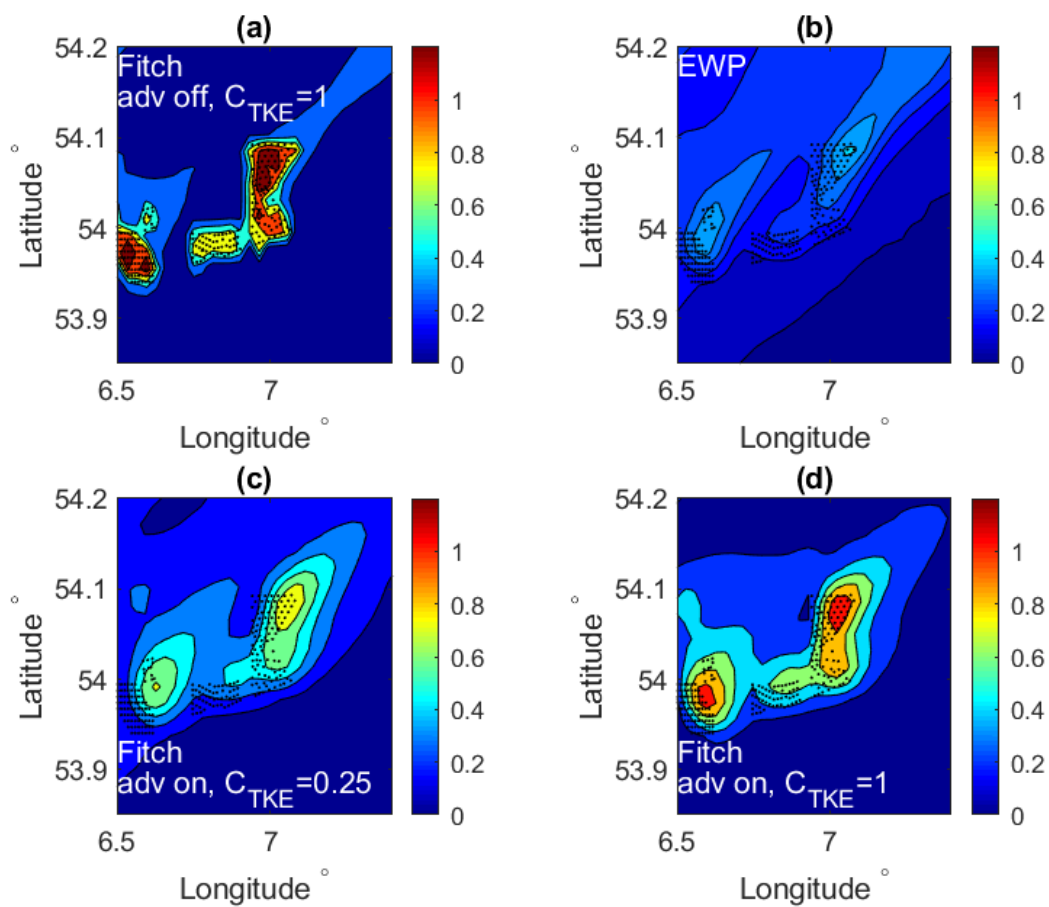
Figure 13. Spatial distribution of TKE at 250 m from WRF model at 20171014 15:30 (a) using Fitch scheme, advection off and $C_{TKE} = 1$; (b) using EWP scheme; (c) using Fitch scheme, with advection on and $C_{TKE} = 0.25$; (d) using Fitch scheme, with advection on and $C_{TKE} = 1$
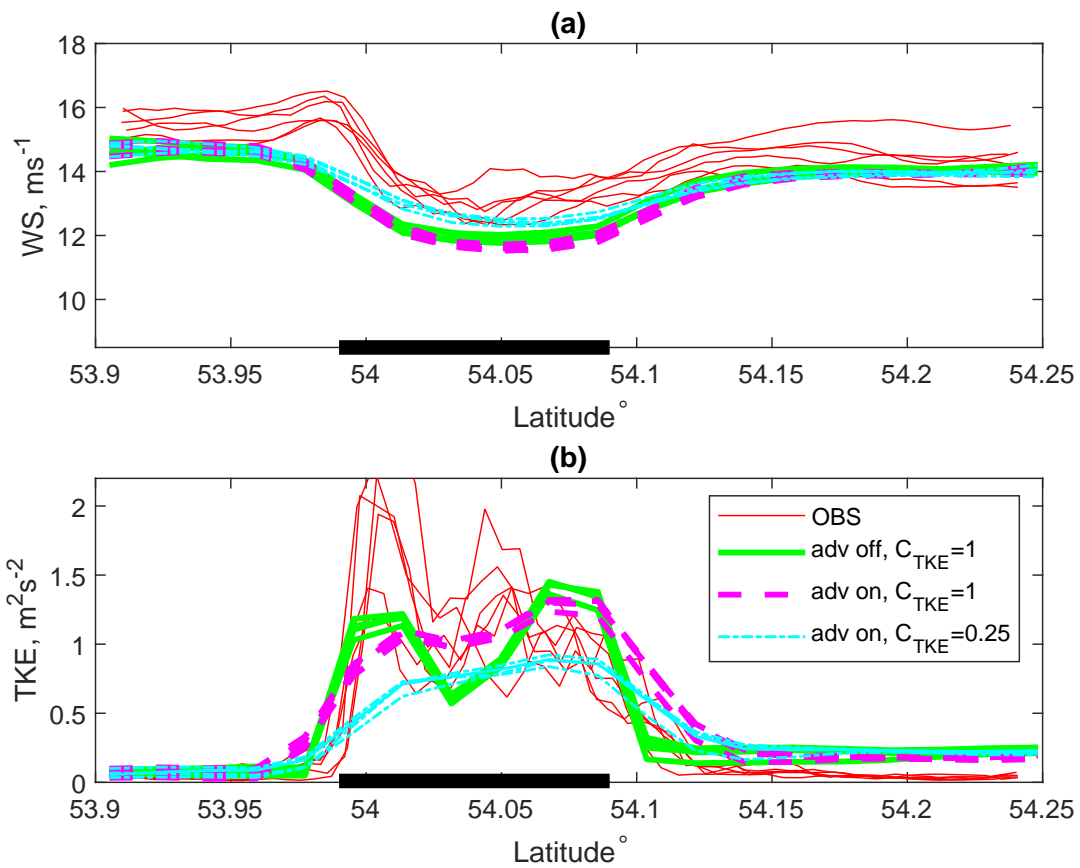
Figure 14. Similar to Fig. 10, comparisions of wind speed and TKE at 250 between measurements and model data from the Fitch scheme, with advection off with $C_{TKE} = 1$, and advection on with $C_{TKE} = 1$ and $C_{TKE} = 0.25$

Table 1. Time of the profile-flights (see track 1-6 in Fig. 2) and transect-flights (see Fig. 2 transect-a).

Flight nr.	start	end
profile 1	2017-10-14 13:22:59.700	2017-10-14 13:25:08.410
profile 2	2017-10-14 14:14:41.600	2017-10-14 14:17:10.470
profile 3	2017-10-14 15:13:31.260	2017-10-14 15:15:53.240
profile 4	2017-10-14 16:10:21.570	2017-10-14 16:12:49.110
profile 5	2017-10-14 16:16:35.240	2017-10-14 16:19:55.230
profile 6	2017-10-14 16:23:22.060	2017-10-14 16:25:05.150
transect 1	2017-10-14 14:20:50.860	2017-10-14 14:30:12.370
transect 2	2017-10-14 14:34:41.180	2017-10-14 14:44:37.520
transect 3	2017-10-14 14:48:27.970	2017-10-14 14:57:43.640
transect 4	2017-10-14 15:01:38.120	2017-10-14 15:11:34.970
transect 5	2017-10-14 15:45:01.130	2017-10-14 15:54:05.160
transect 6	2017-10-14 15:58:29.630	2017-10-14 16:08:34.810

Table 2. Wind farm details for all simulated wind farms.

Wind farm	Turbines	Turbine Model	Hub height [m]	Rotor top [m]	Wind Farm Area [km^2]
Alpha Ventus	12	M5000-116	90	148	4
Amrumbank West	80	SWT-3.6-120	90	150	30
BARD Offshore	80	M5000-116	90	148	59
Borkum Riffgrund 1	78	SWT-4.0-120	87	147	36
Butendiek	80	SWT-3.6-120	91	151	31
Gemini	150	SWT-4.0-130	95	160	68
Global Tech I	80	M5000-116	92	150	40
Gode Wind 1	55	SWT-6.0-154	110	187	40
Gode Wind 2	42	SWT-6.0-154	110	187	29
Horns Rev I	80	V80-2.0	70	110	21
Horns Rev II	91	SWT-2.3-93	55	102	33
Meerwind Süd/Ost	80	SWT-3.6-120	89	149	40
Nordsee One	54	6.2M126_90	90	153	30
OWP Nordergründe	18	6.2M126_84	84	147	3
OWP Nordsee Ost	48	6.2M126_95	96	159	36
OWP Veja Mate	67	SWT-6.0-154	103	180	51
Offshore Windfarm DanTysk	80	SWT-3.6-120	88	148	65
Offshore Windfarm Sandbank	72	SWT-4.0-130	95	159	47
Offshore Windpark Riffgat	30	SWT-3.6-120	90	150	6
Trianel Windpark Borkum	40	M5000-116	92	150	23